Elucidating the Mechanistic Origins of Photocatalytic Hydrogen Evolution Mediated by MoS_2/CdS Quantum-Dot Heterostructures

Junsang Cho,[a]† Nuwanthi S. Suwandaratne,[b]† Sara Abdel Razek,[c] Yun-Hyuk Choi,[a,d] Louis F. J. Piper,[c]* David F. Watson,[b]* Sarbajit Banerjee*[a]

[a]Departments of Chemistry and Materials Science and Engineering, Texas A&M University, College Station, TX 77842-3012 (USA)
[b]Department of Chemistry, University at Buffalo, The State University of New York, Buffalo, NY 14260-3000 (USA)
[c]Department of Physics, Applied Physics and Astronomy, Binghamton University, Binghamton, New York 13902, USA
[d]Department of Materials Science and Engineering, Catholic University of Daegu, Gyeongsan-si, Gyeongbuk 38430 ,South Korea

† These authors contributed equally.

Corresponding Authors: lpiper@binghamton.edu; dwatson3@buffalo.edu; banerjee@chem.tamu.edu

Abstract

Solar fuel generation mediated by semiconductor heterostructures represents a promising strategy for sustainable energy conversion and storage. The design of semiconductor heterostructures for photocatalytic energy conversion requires the separation of photogenerated charge carriers in real space and their delivery to active catalytic sites at the appropriate overpotentials to initiate redox reactions. Operation of the desired sequence of desired light harvesting, charge separation, and charge transport events within heterostructures is governed by the thermodynamic energy offsets of the two components and their photoexcited charge-transfer reactivity, which determine the extent to which desirable processes can outcompete unproductive recombination channels. Here, we map energetic offsets and track the dynamics of electron transfer in MoS_2/CdS architectures, prepared by interfacing two-dimensional MoS_2 nanosheets with CdS quantum dots (QDs), and correlate the observed charge separation to photocatalytic activity in the hydrogen evolution reaction. The energetic offsets between MoS_2 and CdS have been determined using energy-variant X-ray photoemission spectroscopy (XPS) in conjunction with density functional theory. A staggered type-II interface is observed, which facilitates electron and hole separation across the interface. Transient absorption spectroscopy measurements demonstrate ultrafast electron injection occurring within sub-5 ps from the CdS QD to MoS_2, allowing for creation of a longer-lived charge-separated state. The increase of electrons in MoS_2 is evidenced with the aid of spectroelectrochemical measurements and by identifying the distinctive signatures of electron—phonon scattering in picosecond-resolution transient absorption spectra. Ultrafast charge separation across the type-II interface of MoS_2/CdS heterostructures enables a high Faradaic efficiency of ca. 99.4 ± 1.2% to be achieved in the hydrogen evolution reaction (HER) and provides a 40-fold increase in the photocatalytic activity of dispersed photocatalysts for H_2 generation. The accurate delineation of thermodynamic driving forces and dynamics of charge transfer suggests a means of engineering ultrafast electron transfer and effective charge separation in order to design viable photocatalytic architectures.

Introduction

Solar fuels that store energy harvested from sunlight in chemical bonds are attractive alternatives to fossil fuels and will be the foundational energy currency of post-carbon economies.[1, 2] The production of solar fuels requires an interconnected cascade of chemical reactions and charge/mass transport processes: absorption of sunlight, charge separation, charge transport to catalytic sites, diffusion of reactants to catalytic sites, and catalyzed redox events.[3-5] Since it is unlikely that a single material can orchestrate this entire sequence of processes in a synchronized manner, attention has focused on designing heterostructures with multiple components that each mediate a subset of the cascade. Semiconductor heterostructures with the appropriate energetic offsets afford the opportunity to separate photogenerated electron—hole pairs while enabling the harvesting of photons across an extended region of the solar spectrum.[5-7] Considerable recent attention has focused on the design of semiconductor heterostructures that deliver electrons or holes to catalytic sites at low overpotentials.[3] [8] MoS_2 has an optical bandgap broadly tunable from 1.2—1.9 eV as a function of layer thickness[9] and has attracted interest as an earth-abundant electrocatalyst for hydrogen evolution[10] [11-13] and CO_2 photoconversion.[14, 15] Interfacing MoS_2 with semiconductor quantum dots (QDs) that have high oscillator strengths provides a means to effectively harvest sunlight and to deliver electrons to the active edge sites of MoS_2. In this article, we examine the thermodynamic energetic offsets and measure the dynamics of charge transfer in heterostructures of few-layered MoS_2 interfaced with CdS QDs, mapping electron transfer from the conduction band edge of photoexcited QDs to the conduction band of MoS_2 and evidencing the stabilization of a charge-separated state .

In order to achieve high solar conversion efficiencies, the thermodynamic driving forces and dynamics of charge transfer need to be engineered to enable the spatial separation of photogenerated electron—hole pairs at ultrafast timescales before they are able to recombine or be annihilated through unproductive relaxation pathways.[3, 16, 17] Engendering the separation of the charge carriers in real space maximizes the probability for their effective utilization in catalytic reactions. The resulting charge-separated states need to be long-lived and the separated electrons/holes further need to be rapidly transported along potential gradients to catalytic sites to mediate redox reactions.[3] Staggered, type-II, band alignments are particularly desirable to drive rapid interfacial charge separation of photogenerated electrons and holes and to enable their localization at opposite ends of binary heterostructures.[18-22] Interfacing MoS_2 with other semiconductor nanocrystals provides a means to tune interfacial energetic offsets and charge transfer dynamics, thereby enabling electron injection and effective solar energy conversion.[3, 23, 24] As an example of this approach, Hong *et al.* have demonstrated that upon photoexcitation of MoS_2/WS_2 heterostructures, charge separation is achieved within 50 fs, enabling a substantially increased photocurrent density and incident-photon-to-current-efficiency in a photovoltaic device.[21, 25] II-VI semiconductors are attractive candidates for coupling with MoS_2 by dint of their high absorption cross-sections in the visible region of the electromagnetic spectrum and the size and compositional tunability of their bandgaps.[26, 27]

In this article, we demonstrate the preparation of few-layered MoS_2/CdS QD heterostructures through ultrasonication-assisted chemical exfoliation of bulk MoS_2, followed subsequently by successive ionic layer adsorption and reaction (SILAR) to enable the heterogeneous nucleation of CdS QDs onto MoS_2 sheets. The thermodynamic driving forces for charge transfer in the heterostructures have been examined by determining the relative band alignments using a combination of soft and hard X-ray photoelectron spectroscopy (XPS and HAXPES). Interfacial charge transfer dynamics have been probed using transient absorption spectroscopy.[3, 17] We observe the stabilization of charge-separated states in MoS_2/CdS QD heterostructures and evidence a rapid increase of electron density in MoS_2 through electron transfer within just a few picoseconds. The strongly enhanced carrier concentration is correlated directly with catalytic activity of these systems in the hydrogen evolution reaction (HER), as measured in photoelectrochemical evaluation of thin films and photocatalytic testing of dispersed photocatalysts. The results elucidate mechanistic understanding of the thermodynamics and kinetics of interfacial charge separation and their coupling with redox catalysis in semiconductor heterostructures, yielding design principles for the construction of Type II architectures for photocatalytic energy conversion.

Results and Discussion

Synthesis and Characterization of MoS_2/CdS QD Heterostructures

Few-layered MoS_2 nanosheets were obtained by the ultrasonication-assisted exfoliation of bulk MoS_2 in dimethylformamide (DMF) for 72 h, as described previously in the literature and sketched in **Figure 1A**.[28, 29] The intercalation of DMF molecules in the galleries of MoS_2 weakens the van der Waals interactions, allowing for the exfoliation of few-layered nanosheets.[29, 30] **Figures 1B—G** exhibit transmission electron microscopy (TEM) images, high-resolution TEM images, STEM images, and selected area electron diffraction (SAED) patterns of the exfoliated bare MoS_2 nanosheets. The bare MoS_2 nanosheets span 20—60 nm in their lateral dimensions. The lattice-resolved HRTEM images reveal an interplanar spacing of 0.270 nm corresponding to the separation between the (100) crystallographic planes of 2H MoS_2. The basal planes of MoS_2 exhibit smooth and continuous electron density contrast with respect to the background (**Figure 1B-D**).[31]

MoS_2/CdS heterostructures were assembled by interfacing the MoS_2 nanosheets with CdS QDs using the SILAR process, wherein alternate immersion of the nanosheets in cationic and anionic precursors promotes heterogeneous nucleation of QDs on the nanosheet surfaces (**Figure 1A**). The hexagonal crystal structures of 2H MoS_2 and wurtzite CdS are conducive to the formation of a lattice-matched interface.[16, 32, 33] **Figures 1E—G** show the decoration of the basal planes of MoS_2 with CdS QDs. **Figure 1F** demonstrates the crystallization of wurtzite CdS QDs onto the surfaces of 2H MoS_2 layers. The false-color HRTEM reconstructed from the SAED reflections of wurtzite CdS and 2H MoS_2 illustrates the deposition of CdS QDs on the MoS_2 nanosheets (**Figure 1G**). The SAED patterns of MoS_2/CdS heterostructures are characterized by diffraction spots indexed to the extended crystalline domains of 2H MoS_2 and diffuse rings derived from randomly oriented CdS QDs adhered to the MoS_2 basal planes. SEM images and energy dispersive X-ray spectroscopy (EDS) data further corroborate the presence of QDs on the MoS_2 surface and demonstrate that they are homogenously dispersed (**Figure S1**).

Figure 1H shows diffuse reflectance (DR) spectra acquired for bare MoS_2 and the MoS_2/CdS heterostructures. The bare MoS_2 nanosheets are characterized by two strong bands centered at 615 and 670 nm. These two bands arise from electronic transitions from the spin-orbit-split valence band edge to the degenerate conduction band.[34,35] The DR spectrum acquired for MoS_2/CdS heterostructures contains these two features but is additionally characterized by a significant increase in apparent absorbance in the range of 450—520 nm, corresponding to the first excitonic absorption of CdS QDs.[16, 36] **Figure 1I** shows the Raman spectra of bare MoS_2 and MoS_2/CdS heterostructures. The former is characterized by two strong Raman bands at 376 and 403 cm^{-1}, which are assigned to E^1_{2g} and A_{1g} lattice vibrational modes of MoS_2.[37, 38] In comparison, MoS_2/CdS heterostructures exhibit additional bands, the most prominent of which is an intense band at 296 cm^{-1}, which can be assigned to the longitudinal optic (LO) phonon mode of wurtzite-structured CdS QDs.[16] A broad band at 592 cm^{-1} derives from the second order (2LO) mode. Characterization of the prepared materials by electron microscopy, electron diffraction, energy dispersive X-ray spectroscopy, DR spectroscopy, and Raman microprobe analysis thus attests to the decoration of the 2H MoS_2 nanosheets with CdS QDs.

Energetic Offsets and Thermodynamic Driving Forces for Charge Separation in MoS_2/CdS QD Heterostructures

The electronic structure of the MoS_2 nanosheets has been examined using soft and hard X-ray photoelectron spectroscopy (XPS/HAXPES) to determine the valence band electronic structure prior to the deposition of QDs (**Figure S2**). Photoionization cross-sections are diminished with increasing incident photon energy; however, this effect tends to be much more pronounced for subshells with higher orbital angular momentum. As such, by comparing XPS and HAXPES spectra acquired at different incident photon energies, the relative orbital contributions of states with *s*, *p*, and *d* character can be deconvoluted.[8] In Figure S2, the spectrum acquired with 6 keV excitation shows a pronounced feature at 14.2 eV that is greatly diminished in the spectrum acquired at 1.5 keV excitation; this feature can thus be assigned to S 3s core states of MoS_2. The valence band XPS/HAXPES spectra have been reproduced by cross-sectional weighting of orbital-projected spectra simulated from DFT GGA calculations of bulk MoS_2 (**Figure S2**). Two distinct regions can be distinguished. The first region has four major features within 1—8 eV that are derived from the hybridization of Mo 4d and S 3p states.[39, 40] The second region between 12—16 eV with a pronounced excitation energy dependence is attributable to S 3s core states. A valence-band to Fermi level offset of 1.2 eV is furthermore identified for bare MoS_2.

XPS valence band spectra of both MoS_2/CdS (x3) and MoS_2/CdS (x5) heterostructures acquired at 0.9 keV are shown in **Figure 2A**. For band alignment studies of the MoS_2/CdS heterostructures, lower-photon-energy XPS was preferred over HAXPES because of increased surface sensitivity to the interface. The XPS spectra of the valence band regions were energy aligned to the semi-core Cd 4d feature at 11 eV.[33] The peak intensity in the 10—13 eV region becomes stronger with increasing number of SILAR cycles from x3 to x5; the observed features are thus assigned to Cd 4d and S 3s states derived from CdS QDs.[16] A similar phenomenon of increasing intensity with number of SILAR cycles is observed at the valence band maximum (VBM), which is found to be primarily derived from the S 3p states of the CdS QDs. **Figure 2A** also shows the offset between the VBM of MoS_2 nanoplatelets and the MoS_2/CdS heterostructures, which is ca. 0.2 eV. This value reflects the energy positioning of S 3p VBM states of CdS QDs above the Mo 4d—S 3p hybrid valence band of MoS_2.

The total density of states (DOS) and orbital projected density of states (PDOS) were calculated individually for CdS and MoS_2. A GGA+U calculation with a $U = 8$ eV value for Cd was used for CdS to account for the localized nature of the Cd 4d semi-core level.[41] The U value was selected to match the experimentally measured Cd 4d energy positioning for CdS QDs at 11 eV.[8]. The resultant PDOS for MoS_2 and CdS were each weighted by their orbital cross-sections at the excitation energy[42] to enable fair comparison with the XPS data. The experimental XPS spectra of the MoS_2/CdS (x3 and x5) heterostructures were successfully reproduced by appropriately scaling the combined energy aligned and cross-sectional weighted PDOS of MoS_2 and CdS (**Figures 2A** and **SX**)A valence band offset of 0.2 eV between the CdS and MoS_2 from our XPS valence band extrapolations was required when combining the weighted density functional theory (DFT) to obtain agreement with the measured spectra. The 0.2 eV valence band offset is furthermore consistent with a previously reported value of 1 eV for the VBM—Fermi level offset measured for CdS QDs. [43]

Figure 2B summarizes the band alignment between monolayer MoS_2 and CdS QDs. The valence band offsets were determined from the XPS/DFT analysis shown in **Figures 2A and SX**, whereas the conduction band alignment was determined by including the reported band gap values of MoS_2 (1.72 eV) and CdS QDs (2.35 eV), as also confirmed by the DR spectra in **Figure 1H**.[43, 44] We used the ionization potential of the CdS to align with the vacuum level in order to relate the measured band edges with the hydrogen and oxygen evolving redox potentials.[17] The normal hydrogen electrode (NHE) is 4.5 eV below the vacuum level.[45] The VBM of both materials are more negative than the redox potential V_{O_2/H_2O}, and the CBMs are more positive than V_{H_2/H^+} which makes this interface more suitable for O^{2-} oxidation and H^+ reduction reactions. The thermodynamic driving force for electron transfer from the CBM of CdS QDs to that of MoS_2 is about 0.6 eV. As a result, photoexcited electrons are expected to be transferred from the CdS QDs to the MoS_2, enabling dihydrogen evolution to occur on MoS_2 sites.

Excited-State Dynamics and Charge Separation in MoS_2/CdS QD Heterostructures

The excited-state relaxation, recombination, and charge-transfer dynamics of MoS_2 and MoS_2/CdS (x3) heterostructures have been investigated using transient absorption spectroscopy at nanosecond and picosecond timescales. **Figure 3** depicts three-dimensional transient absorbance (TA) color maps acquired at pump—probe delay times of 0—1000 ns following 360 nm excitation (Figures 3A and B), differential absorbance (ΔA) spectra collected at various delay times from 5—1000 ns (Figures 3C and D), and bleach decay kinetics acquired at three different probe wavelengths (Figures 3E and F) for bare MoS_2 (**Figures 3A**,**C**,**E**) and MoS_2/CdS QD heterostructures (**Figures 3B**,**D**,**F**). Based on the DR spectra plotted in **Figure 1H**, both the MoS_2 nanosheets and the CdS QDs have a strong absorption cross-section at the 360 nm (3.44 eV) excitation wavelength, which as per Figure 2 corresponds to an above-bandgap excitation for both components. **Figures 3A** and **B** exhibit three distinctive induced absorption bands (marked in red) at 480—580, 630—660, and 690—900 nm, respectively, for both the bare MoS_2 and MoS_2/CdS heterostructures as well as transient bleaches (marked in blue) at 430—480, 590—630, and 660—690 nm, consistent with previous observations for MoS_2.[34, 35] The transient bleach features are attributed primarily to ground state depopulation, whereas the induced absorption bands, red-shifted relative to the excitonic bleaches, are attributed to broadening of excitonic features and transient band-gap renormalization induced by population of a continuum of Mo 4*d*—S 3*p* states at the bottom of the conduction band of MoS_2 upon above-bandgap excitation.[12 34, 46] The bleach features are examined in detail since the induced absorption and bleach both result from the same carrier-induced state-filling and electronic structure-perturbing processes.[47]

The high-energy bleach centered at 450 nm is ascribed to the band-nesting transition from the deep valence band of MoS_2 to the conduction band minimum (assigned as the C exciton).[34, 48] The low-energy bleach features centered at 615 and 675 nm are assigned to direct band-gap transitions from the spin-orbit-split valence band maximum of MoS_2 to the degenerate conduction band minimum (assigned as B and A excitons, respectively).[34, 48] **Figures 3C** and **D** show time-dependent differential absorbance (ΔA) spectra collected at various delay times, which indeed show some stark differences between bare MoS_2 and the MoS_2/CdS QD heterostructures. The ΔA intensity of the induced absorption band from 480—550 nm acquired within 1000 ns is significantly decreased for the heterostructures as compared to bare MoS_2. The significant reduction in the induced absorption band at 480—550 nm is primarily ascribed to spectral overlap of the induced absorption band of MoS_2 with the first excitonic bleach of CdS QDs (which has not entirely decayed within this timescale). Indeed previous TA measurements of SILAR-derived β-$Pb_xV_2O_5$/CdS heterostructures have shown the first excitonic bleach of CdS-containing heterostructures to occur in the range of 480—520 nm.[16, 17, 33]

Whilst TA spectra of MoS_2 and the MoS_2/CdS QD heterostructures exhibit similar spectral features, a marked difference is observed in the bleach recovery kinetics. **Figures 3E** and **F** plot bleach recovery traces extracted in wavelength ranges from 460—475 nm (C exciton), 610—615 nm (B exciton), and 670—675 nm (A exciton) for bare MoS_2 and MoS_2/CdS QD heterostructures, respectively. The bleach recovery kinetics reflect the excited-state carrier relaxation dynamics, which encompasses relaxation pathways stemming from 1) charge trapping, 2) radiative recombination, and 3) non-radiative recombination.[34, 35] For both B and A excitons, the bleach recovery kinetics are similar in bare MoS_2 and MoS_2/CdS QD heterostructures with a timescale on the order of 5–200 ns; the similar temporal evolution of both bands is explicable considering that both excitonic features derive from electronic transitions from the spin-orbit-split valence band to the conduction band.[35]

Comparing the recovery kinetics of the bleach features for bare MoS_2 and MoS_2/CdS QDs, the average recombination lifetimes for bare MoS_2 are deduced to be 36.4±4.9 ns (C exciton), 46.1±6.3 ns (B exciton), and 130.5±15.2 ns (A exciton) (**Table S1**). The heterostructures show somewhat increased recombination lifetimes, 43.0±14.2 s (C exciton), 75.6±9.4 s (B exciton), and 173.8±21.4 ns (A exciton). The average lifetime of individual bleach features is increased around by 1.5-fold for the MoS_2 heterostructures relative to bare MoS_2 (**Table S1**). The increased lifetimes are consistent with interfacial separation of electron—hole pairs in the Type II heterostructures[24] and the surface passivation of few-layered MoS_2 with CdS QDs.[16] As per the band alignment diagram deduced in **Figure 2B**, photo-generated holes are expected to be localized on the valence band of CdS, whereas photo-generated electrons are localized in the conduction band of MoS_2. In addition, coordinatively undersaturated defect states within MoS_2 may be passivated by interfacing with QDs, which can effectively circumvent charge trapping by surface-defect states, thereby blocking surface-defect-mediated recombination pathways.

Ultrafast TA spectra have been acquired to resolve excited-state charge separation at the interface between MoS_2 nanosheets and CdS QDs on picosecond timescales. **Figure 4** shows TA intensity maps, differential absorbance spectra, and bleach recovery kinetics contrasting bare MoS_2 (**Figures 4A**,**C**,**G**) and MoS_2/CdS heterostructures (**Figures 4B**,**D**,**H**). The three distinctive excitonic bleaches characteristic of MoS_2 are once again the most dominant spectral features. Upon interfacing MoS_2 with CdS QDs, a pronounced bleach attributable to CdS QDs is evidenced at early timescales in the probe wavelength range of 470—550 nm (**Figure 4B**). As a result of this bleach, the induced absorption band of heterostructures in the wavelength of 470—600 nm is considerably diminished in intensity, as also observed in nanosecond TA spectra (Figures 3B and D). **Figure S3** shows a magnified view of the TA 3D intensity maps from 0—2 ps, clearly demarcating the excitonic bleach from CdS QDs centered at 490 nm (denoted by a dotted-lined circle). The first-excitonic bleach of CdS QDs is dominated by the excited-state electron population. The recovery of the bleach, within several picoseconds after excitation and much more rapidly than for free dispersed CdS QDs, is thus attributable to the transfer of electrons from CdS QDs into the conduction band of MoS_2.

The kinetics of bleach recovery have been extracted by fitting the time-resolved ΔA intensities at 500 nm for both MoS_2 and the MoS_2/CdS heterostructures using multiple exponentials (**Figure S4**). The excitonic bleach of CdS QDs decay rapidly with a lifetime of 4.6 ± 1.5 ps (Figure S4), suggesting rapid excited-state electron injection from CdS to MoS_2. This observation is consistent with time-dependent DFT calculations by Zhang and co-workers, which have determined that the Cd-terminated (001) surface of CdS forms an energy matched interface with MoS_2, allowing for ultrafast level crossing of photoexcited carrier states in CdS with receiving states in MoS_2. The electron transfer pathway accessible in this system mitigates the need for slower phonon-mediated processes and is posited to be key to the effective catalytic utilization of photogenerated electrons in MoS_2/CdS heterostructures.

Intriguingly, the B and A excitonic bleaches of MoS_2 blue-shift and narrow within several picoseconds after pulsed excitation. **Figures 4E** and **F** contrast the time-dependent blue-shifting of the wavelength of bleach minimum (most negative ΔA) (λ_{bleach}), the magnitude of the blue shift relative to its initial position at 0.5 ps (ΔE; meV), as well as change in FWHM (eV) of the bleach features at 615 nm and 675 nm corresponding to the B and A excitons, respectively, for bare MoS_2 and MoS_2/CdS heterostructures. Within approximately 20 picoseconds, the B excitonic bleach of MoS_2 is blue-shifted from 613 to 610 nm (ΔE = 12.9 meV), whereas the A exciton is blue-shifted from 673 to 670 nm (ΔE = 8 meV).[47] The blue-shifting of the B an A excitonic bleaches for bare MoS_2 is associated with the decay of excited state carriers through inelastic exciton—phonon scattering.[48, 49] In the highly symmetric hexagonal Brillouin zone of 2D transition metal dichalcogenides, there are multiple possible electron scattering channels wherein excited charge carriers can couple with associated phonon modes through intervalley as well as intravalley scattering processes.[48, 49] The blue-shift of the bleach features corresponding to valence-to-conduction band transitions reflects strong coupling of the electronic transitions with phonon modes, which allows for relaxation of energy and momentum conservation.[48]

Further evidence for the blue-shift of excitonic features representing an accumulation of electron density in MoS_2 comes from spectroelectrochemical measurements shown in **Figure 5**. Ground-state absorption spectra of MoS_2 films on FTO electrodes have been acquired under the application of either an oxidizing or reducing potential (**Figure 5A**). Ground-state differential absorbance spectra were computed by subtracting the absorption spectrum of the neutral sample from the absorption spectrum of the oxidized or reduced sample. Spectra of both oxidized and reduced samples comprise distinctive bleach features at 600—615 and 670—680 nm. However, the spectrum of reduced MoS_2 spectrum is slightly blue-shifted relative to that of oxidized MoS_2. Moreover, induced absorption features are observed at 640 and 690 nm in the spectrum of reduced MoS_2. Importantly, the TA spectrum of photoexcited MoS_2 is accurately modeled as a linear combination of the absorbance difference spectra associated with electrochemically reduced and oxidized MoS_2 (**Figure 5B**). As such, the blue shift of excitonic bleaches serves as a reliable indication of electron density in the conduction band of MoS_2.

Notably, TA spectra of the MoS_2/CdS heterostructures (top and middle panels of **Figures 4E** and **F**, top and middle panels) exhibit a more pronounced blue-shift of the B and A excitonic bleaches relative to bare MoS_2. The bleach features of the heterostructures are blue-shifted from 621 to 615 nm (ΔE = 19.1 meV) for the B exciton and from 678 to 674 nm (ΔE = 9.5 meV) for the A exciton. The more pronounced blue-shift of bleach features for heterostuctures reflects an increased electron concentration as a result of photoexcited electron transfer from CdS QD to MoS_2. The higher carrier density brings about stronger electron—phonon coupling within the heterostructures. Thus, the TA spectra provide evidence for ultrafast directional electron transfer that results in the localization of electrons in of MoS_2 and holes in CdS.[21, 48] The exciton-phonon scattering has further been evidenced by investigating the change in the full-width-at-half-maximum (FWHM) of the excitonic bands over time; the broadening of the bands is strongly indicative of phonon scattering processes (bottom panel to **Figures 4E** and **F**).[49] In TA spectra obtained at 0.5 ps, the excitonic bleaches are broader for the MoS_2/CdS heterostructures (FWHM of 125 and 90 meV for B and A excitons, respectively) than for bare MoS_2 (FWHM of 96 and 65 meV for B and A excitons, respectively). The broadening of the excitonic bands further attests to the increased carrier density in MoS_2 resulting from ultrafast electron transfer from CdS QDs to MoS_2. The FWHM of both MoS_2 and heterostructures is gradually decreased in the 1000 ps measured time interval as the photoexcited carriers undergo charge recombination, thereby reducing electron—phonon scattering within the system.

The recovery kinetics of the excitonic bleach features have been further analyzed to examine the excited-state dynamics for both the bare MoS_2 and the MoS_2/CdS heterostructures. The bleach recovery kinetic traces were fitted with multiexponential functions (**Figures 4G** and **H**); fitting parameters are in Table S2. For both bare MoS_2 and MoS_2/CdS heterostructures, the B and A excitonic bleaches decay more slowly than the C excitonic bleach, which is attributed to the ultrafast intraband relaxation process accessible for the latter. Notably, all three bleaches recover more slowly for the heterostructures than for bare MoS_2. Average lifetimes from multiexponential fits are 26.7±1.1, 71.5±4.2, and 11.1±2.0 ps for C, B, and A excitons, respectively, for bare MoS_2, and are increased to 47.1±1.4, 79.6±1.9, and 107.2±2.6 ps, respectively, for MoS_2/CdS heterostructures. The recovery of the bleach features results from charge-carrier trapping by surface trap states occurring within 1—5 ps; defect-assisted nonradiative recombination including carrier—phonon scattering and Auger scattering, occurring on time scales of up to 100 ps; and direct electron-hole recombination occurring at timescales of ca. 1000 ps.[34, 35, 47, 50, 51] The increased lifetime of the heterostructures is primarily attributed to blocking of the fastest relaxation channel as a result of surface passivation of MoS_2 with

CdS QDs as well as improved charge separation consistent with type II band alignment utilizing the electron transfer process accessible within these heterostructures.[16, 36]

Photoelectrochemical Characterization and Photocatalytic Evaluation of MoS_2/CdS Heterostructures.

We performed photoelectrochemical experiments to examine whether excited-state charge separation at MoS_2/CdS interfaces, facilitated by ultrafast electron transfer between energetically matched states in the conduction bands of the two components (**Figure S4**), could be exploited in redox photocatalysis. Thin films of MoS_2/CdS-QD heterostructures or bare MoS_2 were deposited onto FTO-coated glass slides to generate working electrodes of three-electrode cells (**Figure 6**). The electrolyte contained lactic acid as a source of protons and a sacrificial reductant. **Figure 6A** contrasts current—potential curves of MoS_2/CdS/FTO and bare-MoS_2/FTO photoelectrodes, obtained from linear sweep voltammetry measurements, from 0 to 0.9 V *versus* SCE under chopped visible-light (400—720 nm) illumination. In control experiments, bare MoS_2-modified electrodes did not exhibit any measurable photocurrent despite the semiconducting nature of MoS_2 (few-layered MoS_2 is an indirect bandgap semiconductor). In contrast, MoS_2/CdS-heterostructure-modified electrodes exhibited well-resolved oxidative photocurrents with an onset approximately 500 mV positive of the dark oxidation current. Average photocurrent amplitudes of 14.6±1.6 μA were obtained for MoS_2/CdS at 0.2 V *versus* SCE. Finally, chronocoulometry experiments were performed, and the generation of H_2 after prolonged white-light illumination of electrodes was measured by sampling the headspace above the cell using gas chromatography. When MoS_2/CdS-modified electrodes were illuminated for 1 h (400—720 nm, 120 $mW\cdot cm^{-2}$) at an applied potential of 0.2 V *vs*. SCE, 0.20 μmol of H_2 was evolved with the consumption of 40 mC of charge, corresponding to an average Faradaic efficiency of 99.4±1.2% (**Figure S5**). Importantly, no H_2 was detected by gas chromatography in control experiments involving (a) MoS_2/CdS-modified electrodes in the absence of illumination or for (b) bare MoS_2 under white-light illumination. Thus, both the type-II interface of the heterostructures and photoexcitation are necessary to catalyze the reduction of protons to hydrogen. Our photoelectrochemical data are consistent with a mechanism wherein light-driven electron transfer from CdS to MoS_2 across the type-II interface yields a charge-separated state. In this mechanism, lactic acid is oxidized at the photoanode, whereas electrons migrate to the dark cathode and reduce protons to H_2 (**Figures 6B** and **C**). This mechanism is supported by XPS/DFT analysis (**Figure 2B**), which reveal the type II energetic offsets, by TA measurements (**Figures 4 and S3**), which provide evidence for ultrafast charge separation and electron accumulation in MoS_2, and by time-dependent DFT calculations of electron transfer at MoS_2/CdS interfaces.

We have further evaluated photocatalytic hydrogen evolution reaction using dispersed MoS_2/CdS-QD heterostructures as photocatalysts. The photocatalytic production of H_2 was evaluated under visible-light irradiation (400—720 nm) using lactic acid as a proton donor and sacrificial reductant. Prolonged illumination of dispersed MoS_2/CdS heterostructures under these conditions resulted in the evolution of H_2 gas at an average rate of 38.6±1.2 $\mu mol\cdot h^{-1}$. Control experiments performed for heterostructures in the absence of light or using bare MoS_2 indicated no production of hydrogen. Prolonged illumination of dispersed CdS QDs resulted in the evolution of H_2 at an average rate of just 1.1±0.025 $\mu mol\cdot h^{-1}$ (**Figure 6D**). Thus, a 40× increase in hydrogen production was observed for CdS/MoS_2 heterostructures as compared to CdS alone and can be attributed to the rapid and efficient photo-induced charge separation across the CdS/MoS_2 interface, which results in the holes being localized in CdS and electrons in MoS_2.[52]

Conclusions

MoS_2/CdS heterostructures with a type-II interface have been prepared through the ultrasonication-assisted chemical exfoliation of bulk MoS_2 followed by SILAR deposition of CdS QDs. The energetic offsets between the two components have been determined by XPS and HAXPES in conjunction with

DFT calculations and suggest a type II band alignment. TA spectroscopy measurements indicate ultrafast charge separation and long-lived charge-separated states in the heterostructures as compared to bare MoS_2. Ultrafast TA spectroscopy measurements support the notion of electron transfer across level-matched states from the conduction band of CdS QDs to the conduction band of MoS_2. A distinctive spectroscopic signature of electron accumulation in MoS_2 has been derived from spectroelectrochemical measurements and shows rapid (sub-5 ps) electron transfer and considerably greater accumulation of electron density in the heterostructures as compared to bare MoS_2. Photoelectrochemical measurements of heterostructure thin films and photocatalytic evaluation of dispersed photocatalysts reveal that the type-II interface underpins effective charge separation, enabling photocatalytic hydrogen evolution at high Faradaic efficiencies. Our results delineate the need for optimal energetic offsets (determined accurately here using variable-energy photoemission measurements), rapid and efficient charge separation (examined using the distinctive spectroscopic signatures of charge separation and electron accumulation), and efficient redox catalysis in the design of photocatalyst heterostructures. SILAR-derived MoS_2/CdS heterostructures show great promise in photocatalytic hydrogen evolution.

Experimental Section

Synthesis of MoS_2 Nanosheets and SILAR Functionalization with CdS QDs

Few-layered MoS_2 nanosheets were prepared through exfoliation of bulk MoS_2 in DMF. In a typical reaction, 1 g of MoS_2 bulk powder with 325 mesh (trace metal basis) was placed in a vial with 50 mL of DMF and the mixture was ultrasonicated for 72 h until the color of the supernatant changed to dark green. The dispersions of MoS_2 nanosheets in DMF were vacuum filtered through a filter paper with pore size of 1 μm to remove the larger unexfoliated particles. The recovered colloidal MoS_2 dispersion in DMF had a concentration of 2—3 mg/mL. Surface functionalization of MoS_2 with CdS QDs was performed using the SILAR process by adapting previously reported methods.[16, 33] In a typical SILAR cycle, CdS QDs were directly grown onto the surfaces of MoS_2 nanosheets by sequentially mixing the MoS_2 nanosheets with a cadmium precursor solution (50 mM $Cd(NO_3)_2\cdot 4H_2O$ in ethanol), followed by a sulfide solution (50 mM $Na_2S\cdot 9H_2O$ in ethanol) in an argon-filled glove bag.[3] After mixing each precursor solution, the MoS_2 nanosheets were washed with ethanol to remove unreacted precursors. The resulting MoS_2/CdS heterostructure samples were collected by centrifugation at 6500 rpm for 90 s and dried overnight under ambient conditions. The subsequent measurements pertain to samples prepared with three successive SILAR cycles, which are denoted as being x3. Five SILAR cycles (x5) were performed to prepare samples for which sulfide-derived electronic states from CdS and MoS_2 were resolvable in photoemission measurements.

Electron Microscopy, Electron Diffraction, and Vibrational Spectroscopy Characterization

Scanning electron microscopy (SEM) and energy dispersive X-ray spectroscopy (EDS) measurements were performed on a FEI Quanta 600 FE-SEM instrument operated at 10 kV. An Oxford EDS system was used to acquire EDS spectra and elemental maps. Samples for SEM measurements were prepared by dispersing the synthesized heterostructure samples onto double-sided carbon tape. High-resolution transmission electron microscopy (HRTEM) and selected area electron diffraction (SAED) measurements were acquired using a FEI Tecnai G2 F20 FE-TEM operated at 200 kV. Samples for TEM measurements were prepared by drop-casting colloidal dispersions of the heterostructures in ethanol onto Formvar/carbon support film on 400 mesh copper grids.

DR measurements were preformed using the Praying Mantis accessory in a Hitachi U-4100 UV-vis-NIR spectrophotometer. The DR spectra were obtained in the range of 200 – 800 nm for all samples at a scan speed of 600 nm/min. Samples for DR analysis were prepared by crushing powder samples with a mortar and pestle into a fine powder, which was placed directly into a microsampling cup that was used within the Praying Mantis Diffuse Reflectance accessory. Raman spectra were obtained for powder samples using a Jobin-Yvon Horiba Labram HR instrument coupled to an Olympus BX41 microscope. The 514.5 nm wavelength from an Ar-ion laser was used as the excitation source. Raman spectra were acquired with spectral resolution of 3 cm^{-1} using a 1800 lines-per-mm grating.

X-ray Photoemission Spectroscopy and Spectral Simulations

Soft X-ray photoelectron spectroscopy (XPS) measurements with an effective probing depth of ca. 4 nm were performed at beamline 29-ID IEX at the Advanced Photon Source of Argonne National Laboratory in Lemont, IL. The beamline is equipped with a variable line spacing plane grating monochromator and a Scienta R4000 hemispherical analyzer. Additional XPS measurements were performed at the Analytical and Diagnostics Laboratory at Binghamton University. HAXPES data were acquired at beamline I09 of the Diamond Light Source at the Harwell Science and Innovation Campus in Oxfordshire, UK.

Density functional theory (DFT) calculations were performed using the WIEN2k software package, which solve the Kohn-Sham equations using a full potential and linearized-augmented planewaves with local orbitals (LAPW+lo) in a self-consistent manner.[53, 54] The generalized gradient approximation of Perdew, Burke and Ernzerhof (GGA-PBE) was used to address the correlation and exchange potentials for MoS_2 cells. GGA+U including electron correlation was used for the CdS cell. The cutoff between core and valence states was set as -6.0 Ry for both systems. The planewave cutoff parameter RKMAX was chosen to be 7.

Transient Absorption Spectroscopy

Ultrafast TA spectra were obtained using a Ti:sapphire amplified laser system (Spectra Physics Spitfire Pro, 800 nm, 1 kHz repetition rate, 100 fs) in conjunction with Helios spectrometers (Ultrafast System) for thin films of samples (using 1 mg/mL MoS_2/CdS dispersion in ethanol spray-coated onto glass microscope slides). Excitation pump pulses with tunable wavelength were generated using an optical parametric amplifier from Light Conversion Ltd. A supercontinuum probe beam in the range of 425—900 nm was created by focusing a fraction of the laser fundamental into a sapphire disc. The probe light was divided into signal and reference beams, both of which were detected on a shot-by-shot basis with fiber-coupled silicon (visible) or InGaAs (infrared) diode arrays. The delay time between pump and probe was mechanically controlled using a motorized delay stage from Newport. Nanosecond TA measurements were performed using the same ultrafast pump pulses along with an electronically delayed supercontinuum light source with a subnanosecond pulse using an EOS spectrometer (Ultrafast Systems). TA decay traces were compiled by averaging ΔA values over a given range of probe wavelengths at each delay time. Decay kinetics trace and fitting are obtained using the following equations (1-2) where the average lifetime of carriers was calculated by dividing the amplitude-weighted lifetime with the pre-exponential weighting factor (A_i).

$$\Delta A = \Delta A_0 + \sum_i A_i e^{\left(-\frac{t}{\tau_i}\right)} \qquad (1)$$

$$\langle \tau \rangle = \frac{\sum_i A_i \tau_i}{\sum_i A_i} \qquad (2)$$

where ΔA is differential absorbance, ΔA_0 is the differential absorbance at the longest timescales, A_i is a pre-exponential weighting factor of the individual component, t is the pump—probe delay time, and τ_i is the lifetime of the individual component. All decay traces of bare MoS_2 nanosheets and MoS_2/QD heterostructures were well fitted using triexponential decay kinetics (i = 3). The best fitting results correspond to those collected using the smallest number of individual decay lifetimes (τ_i) with the minimum χ^2 for the fit.[36] The parameters extracted from fitting multiexponential decay kinetics are tabulated in **Tables S1** and **S2**.

Photoelectrochemical Measurements

Photoelectrochemical measurements, including linear sweep voltammetry and chronocoulometry, were acquired using a Princeton Applied Research (PAR) VersaSTAT 3 potentiostat. Data were acquired at room temperature using a custom-built, air-tight three-compartment electrochemical cell with CdS/MoS_2-modified fluorine-doped tin oxide (FTO) or MoS_2-modified FTO as the working electrode, a coiled Pt wire as the counter electrode, and saturated calomel electrode (SCE) as the reference electrode. The electrolyte solution comprised a 0.2 M solution of KNO_3 and a 0.1 M solution of lactic acid dissolved in a 1:4 (*v*:*v*) water:acetonitrile mixture with a measured pH of 3. Linear sweep voltammograms were measured at a scan rate of 10 $mV{\cdot}s^{-1}$ under manually chopped illumination (5 s on/off). For experiments in which H_2 generation was quantified, the electrochemical cell was first purged with Ar for 30 min. The illumination source was a 100 W Xe arc lamp (Oriel 133 Photomax) equipped with a filter transmitting light from 400 to 720 nm (120 $mW{\cdot}cm^{-2}$).

Quantitative Analysis of H_2 Generation

For gas quantification, a 3 mL aliquot was extracted from the headspace above the electrolyte using a 10 mL gastight syringe and was analyzed using a Perkin Elmer Clarus 580 gas chromatograph with a thermal conductivity detector using Ar as the carrier gas. The Faradaic efficiency was calculated using the following equation (3):

$$\text{Faradaic efficiency (\%)} = \frac{[\text{H2 produced (mol)} \times 2 \times 96{,}485\ (\text{C/mol})]}{\text{Charge passed during electrolysis (C)}} \times 100\% \qquad (3)$$

Photocatalytic H_2 Generation

Photocatalysis experiments were performed using a 100 mL Pyrex flask at ambient temperature and atmospheric pressure. The flask was sealed with a silicone rubber septum. The light source was a 100 W Xe arc lamp (Oriel 133, Photomax); a filter transmitting 400 to 720 nm light was used to modulate the irradiance and was positioned 20 cm away from the photocatalytic reactor. The measured intensity at the flask was determined to be 120 $mW{\cdot}cm^{-2}$. The photocatalyst (50 mg) was suspended in a 50 mL mixed solution of lactic acid (LA, 20 vol.%) and water under magnetic stirring. For control experiments, bare MoS_2 (50 mg) and precipitated CdS QDs (50 mg) were examined under same conditions. Before irradiation, the suspensions were deaerated with Ar for 30 min to remove dissolved oxygen. Magnetic stirring was used in order to keep the photocatalyst particles in suspension. After 1 h of illumination, gas (3 mL) was sampled from the headspace above the reaction mixture and was analyzed as described above using a gas chromatograph (Perkin Elmer Clarus 580) equipped with a thermal conductivity detector with Ar as the carrier gas.

Spectroelectrochemistry Experiments

To observe changes in the absorption spectra resulting from oxidation or reduction, spectroelectrochemical experiments were performed. A one-compartment, three-electrode electrochemical cell (quartz cuvette, 1 cm path length, with a 24/40 ground glass joint connection) was used with a working electrode (spray-coated MoS_2 on FTO-coated glass slides), a Pt mesh counter electrode, and a SCE reference electrode. Electrochemical measurements were performed using a PAR VersaSTAT 3 potentiostat. The electrolyte was 0.1 M tetrabutylammonium perchlorate (Alfa Aesar, electrochemical grade) in anhydrous acetonitrile (EMD). The entire cell assembly was housed on the sample stage of the spectrophotometer so that absorption spectra could be obtained while performing electrochemical measurements. An oxidizing potential of +1.5 V (*vs*. SCE) and a reducing potential of −0.25 V (*vs*. SCE) was applied to two separate MoS_2 films. Absorbance spectra of the oxidized and reduced films were obtained after applying a potential for 5 min. Differential absorbance spectra were obtained by subtracting the absorbance spectrum of the neutral sample from the absorbance spectrum of the oxidized or reduced sample.

Acknowledgements

This work was supported by the National Science Foundation under DMREF 1627197, DMREF 1626967, and DMREF 1627583. We also thank beamline scientists, Dr Tien-Lin Lee (Diamond Light Source) and Fanny Rodolakis (Advanced Photon Source) for their assistance with the photoemission experiments. We acknowledge Diamond Light Source for time on Beamline I09 under Proposals SI22148. This research used resources of the Advanced Photon Source, a U.S. DOE Office of Science User Facility operated for the DOE Office of Science by Argonne National Laboratory under Contract No. DE-AC02-06CH11357. Transient absorption measurements were performed using resources of the Center for Functional Nanomaterials, which is a U.S. DOE Office of Science Facility, at Brookhaven National Laboratory under contract No. DE-SC0012704. We thank Matthew Sfeir for his assistance with transient absorption measurements. We thank Professor David Lacy and Karthika Kadassery (Buffalo) for their guidance in the use of gas chromatography to quantify evolved hydrogen.

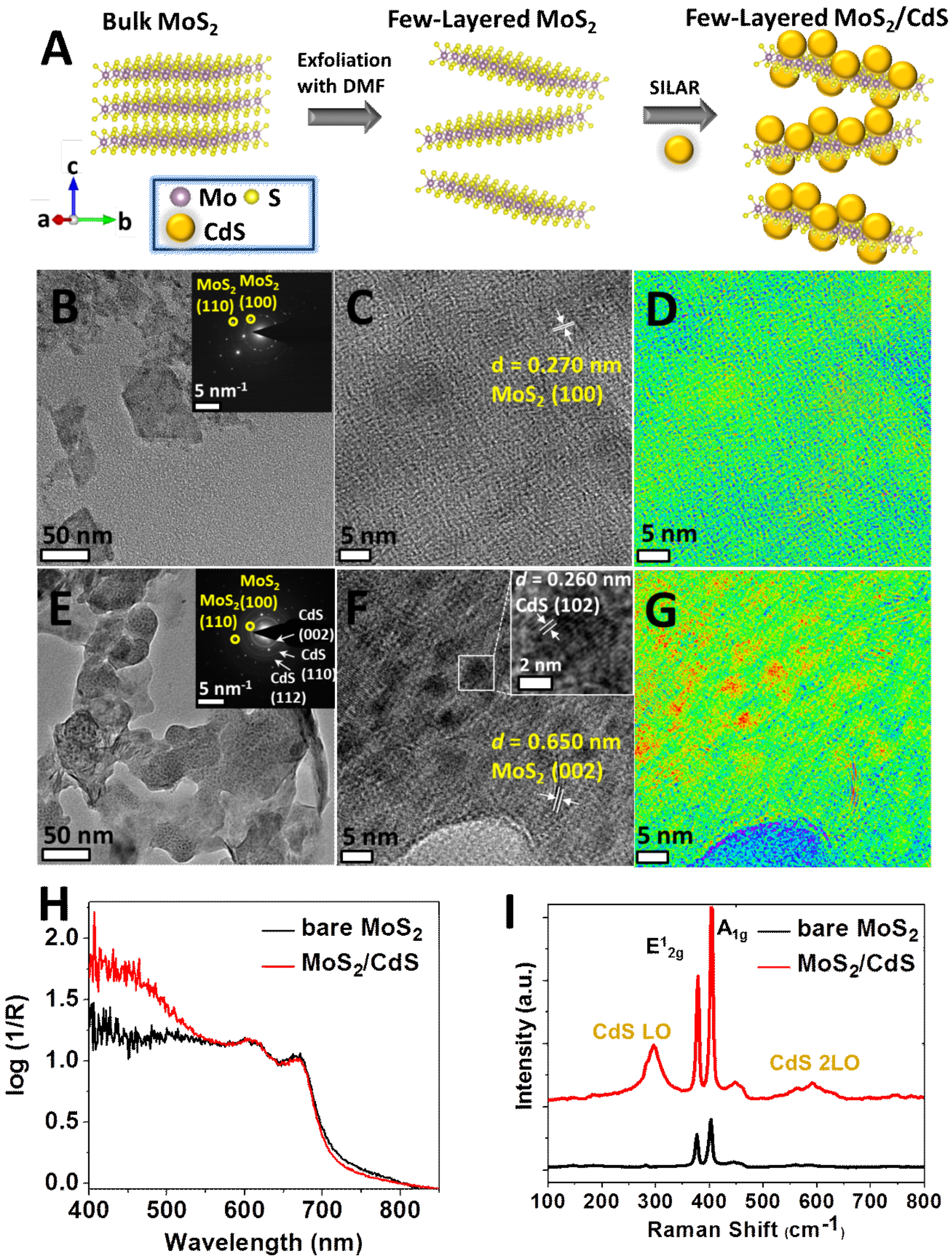

Figure 1. Interfacing MoS$_2$ nanosheets with CdS QDs. A) Schematic illustration of the preparation of few-layered MoS$_2$ by chemical exfoliation followed by the deposition of CdS QDs by SILAR. B) TEM image of exfoliated MoS$_2$ nanosheets; the inset shows a SAED pattern, which has been indexed to the 2H phase of MoS$_2$ (PDF# 06-0097). C) HRTEM image of MoS$_2$ nanosheets showing the separation between the (100) planes of 2H MoS$_2$. D) False-color image constructed using the SAED reflection indexed to the (002) planes of the 2H polymorph of MoS$_2$. E) Low-magnification TEM image showing the speckled appearance of MoS$_2$ after decoration with CdS QDs; the inset shows an indexed SAED pattern with spots and diffuse rings indexed to the 2H polymorph of MoS$_2$ (PDF# 06-0097) and the

wurtzite polymorph of CdS (JCPDS# 41-1049). F) Lattice-resolved image of CdS QDs within MoS_2/CdS heterostructures; the observed lattice spacing derives from the separation between the (102) planes of CdS QDs, which is clearly distinguishable from the lattice spacing of 0.65 nm corresponding to the separation between the (002) planes of lamellar-structured MoS_2.[31] G) False-color map reconstructed from reflections characteristic of CdS QDs and MoS_2 nanosheets; the former is shown in red/yellow whereas MoS_2 substrate is delineated in cyan/blue. H) DR and I) Raman spectra for bare MoS_2 and MoS_2/CdS heterostructures; the DR spectra are normalized to the reflectance band at 675 nm (solely derived from MoS_2) to facilitate comparison.

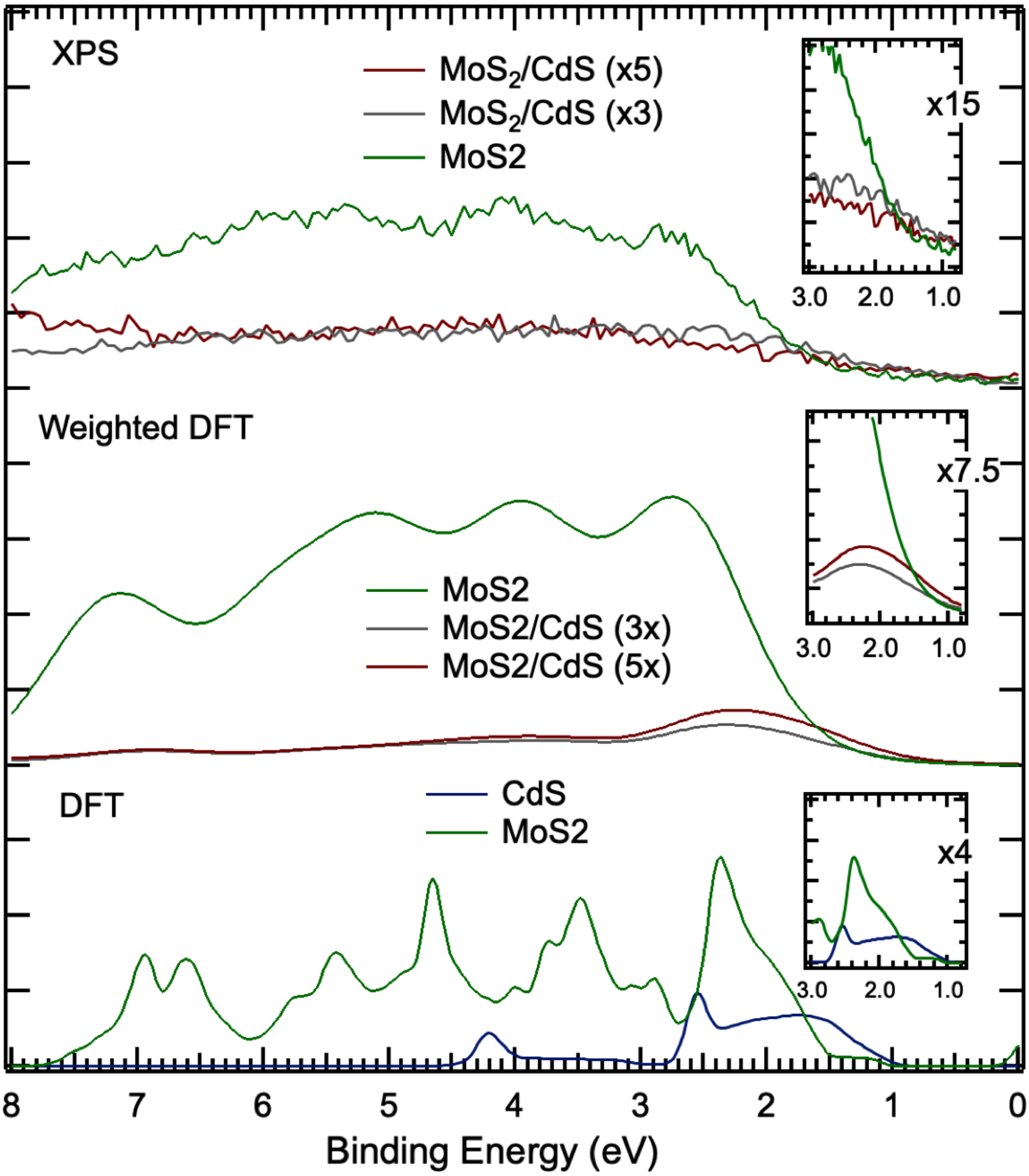

Figure 2. Determination of Energetic Offsets of MoS_2/CdS QD Heterostructures. A) Measured valence

band spectra from XPS of MoS_2 with MoS_2/CdS (x3), and MoS_2/CdS (x5) heterostructures compared with weighted DFT with a VB offset of 0.2 eV between MoS_2 and CdS. B) Measured band alignment of the MoS_2 nanoplatelets and CdS QDs with respect to vacuum level and water oxidation/hydrogen evolution potentials.

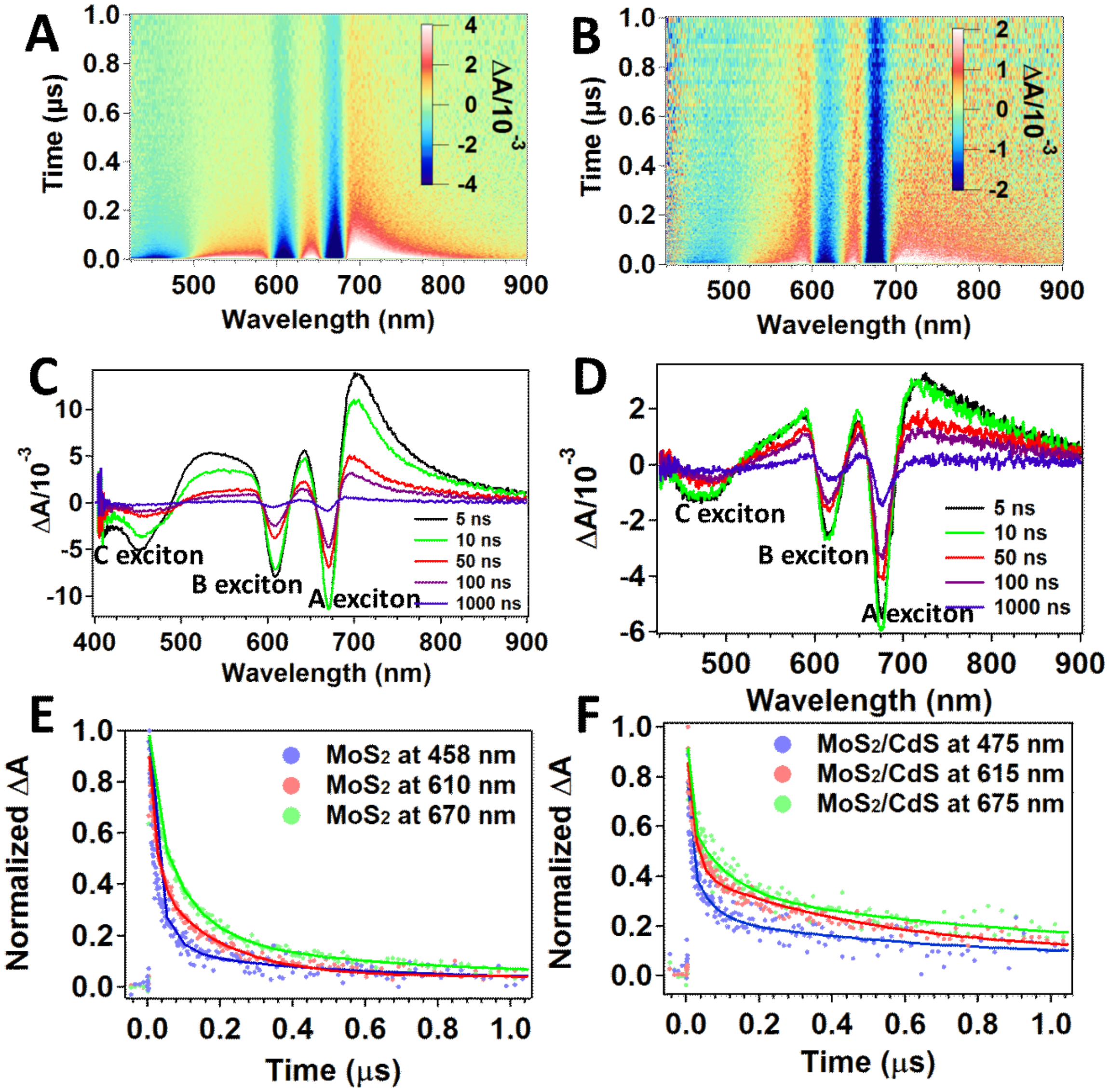

Figure 3. Nanosceond TA spectra of MoS_2/CdS heterostructures. A,B) Three-dimensional (3D) TA color maps (top) acquired with 0—1000 ns delay times at probe wavelengths of 400—900 nm after a pump excitation of 360 nm for A) bare MoS_2 and B) MoS_2/CdS heterostructures. C,D) TA spectra collected at delay times of 5, 10, 50, 100, 500, and 1000 ns for C) bare MoS_2 and D) MoS_2/CdS heterostructures. E,F) Bleach recovery traces and triexponential fits for E) bare MoS_2 and F) MoS_2/CdS heterostructures at the probe wavelengths corresponding to C (458—475 nm), B (610—615 nm), and A excitons (670—675 nm). The fitting parameters are listed in Table S1.

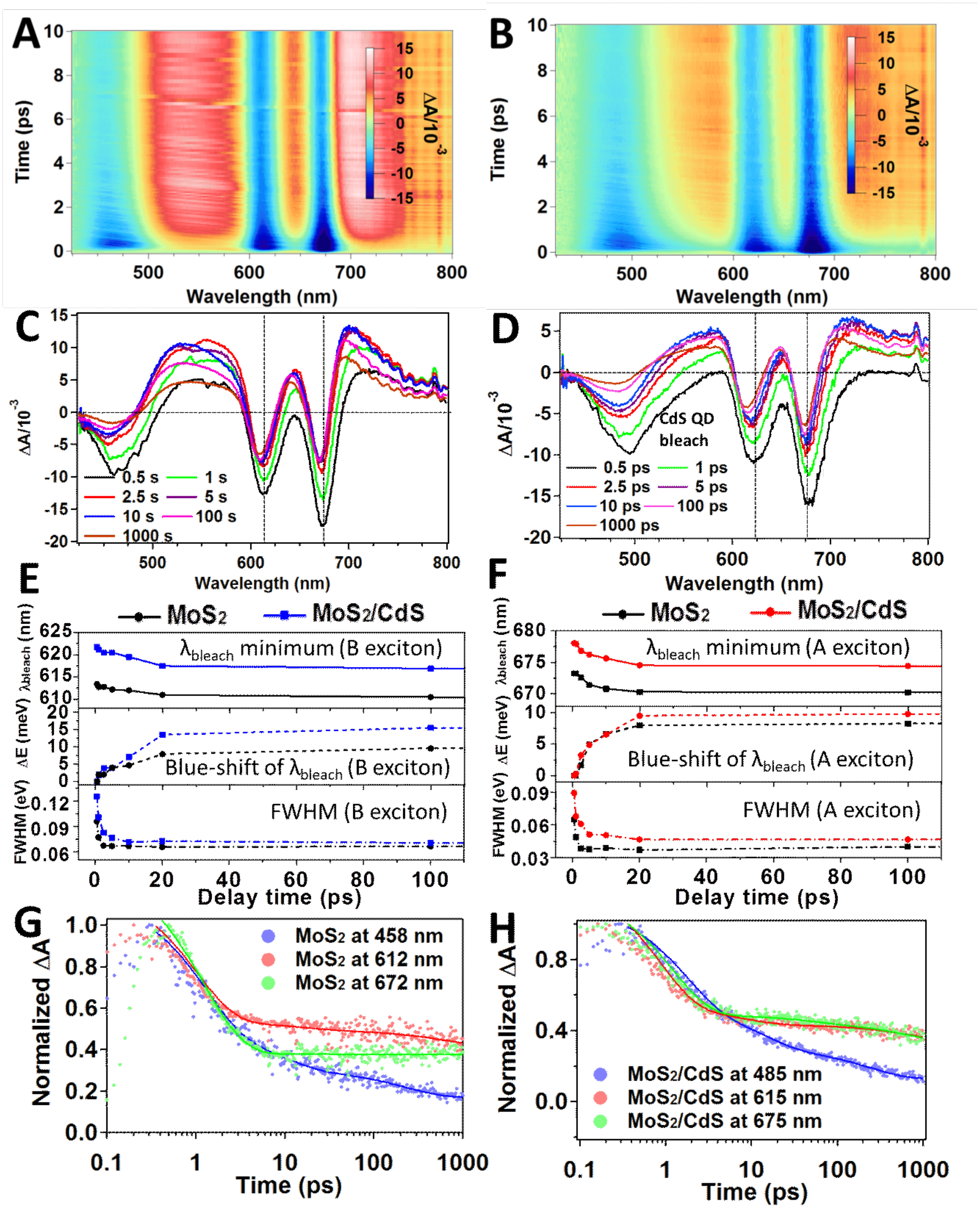

Figure 4. Ultrafast Charge Transfer Dynamics. A,B) Three-dimensional TA color maps in the range of 0—10 ps across a probe wavelength range of 425—800 nm acquired for A) MoS_2 and B) MoS_2/CdS heterostructures after 360 nm pump excitation. TA spectra collected upon initial pump excitation at 360 nm at delay times of 0.5, 1, 2.5, 5, 10, 20, 100, 500, and 1000 ps for C) MoS_2 and D) MoS_2/CdS heterostructures. Plot of the position of the bleach minimum (top panel), blue-shift in differential energy (middle panel), full-width-at-half-maximum change (bottom) measured across a time interval of 1000 ps from initial excitation for E) MoS_2 and F) MoS_2/CdS heterostructures. G,H) Evolution of bleach intensity as a function of time and fitting to kinetic expressions for G) MoS_2 and H) MoS_2/CdS

heterostructures at different probe wavelength corresponding to C (458—485 nm), B (612—615 nm), and A excitons (672—675 nm). The extracted fitting parameters are listed in Table S2.

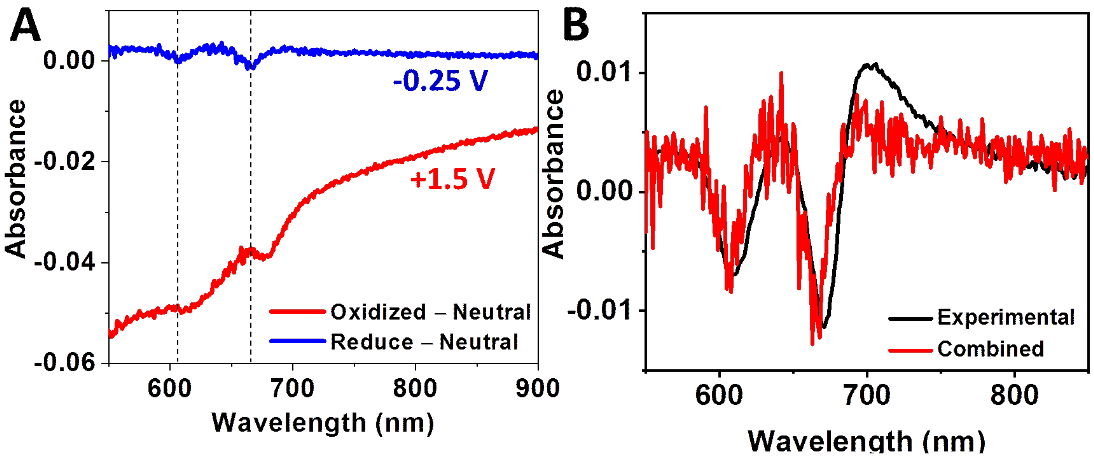

Figure 5. Spectroelectrochemical Evidence of Blue-shifted Excitonic Features of MoS_2 upon Electron Accumulation. A) Spectroelectrochemical absorbance difference spectra of bare MoS_2 obtained at an oxidative potential of +1.5 V (red) and a reduced potential of -0.25 V (blue). B) Nanosecond TA spectrum of bare MoS_2 (black) and fit of spectrum to a linear combination of oxidized and reduced MoS_2 (red) as derived from spectroelectrochemical measurements. The differential spectra in panel A are obtained by subtracting the spectra at the applied potential with the spectra obtained at a neutral potential. The dotted lines indicate the wavelength of B, A excitons with pronounced blue-shift as compared to those at neutral condition.

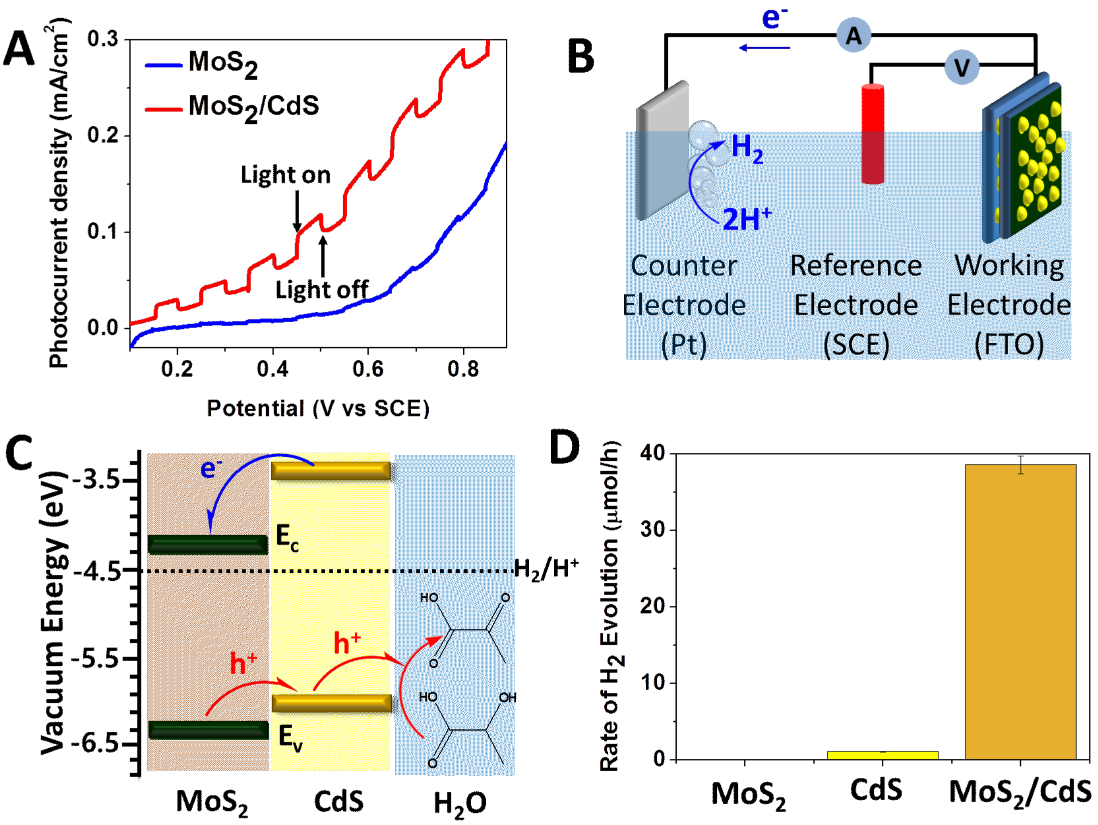

Figure 6. Photoelectrical and Photocatalytic Measurements Evidencing Utilization of Charge-Separated Carriers in Redox Catalysis. A) Linear sweep voltammograms of three-electrode cells with MoS_2/CdS-modified (red) and bare MoS_2-modified (blue) FTO-coated glass working electrodes. The voltammograms have been acquired under chopped white-light illumination in solutions of KNO_3 (0.2 M) and lactic acid (0.1 M) dissolved in a 1:4 (*v*/*v*) mixture of water:acetonitrile (pH = 3). B) Schematic diagram of three-electrode cell configuration. C) Schematic illustration of charge carrier separation in MoS_2/CdS heterostructures. D) Photocatalytic hydrogen evolution for comparison of the rates of photocatalytic H_2 evolution, as determined by gas chromatography, using MoS_2, CdS, and MoS_2/CdS samples dispersed in a 20% (*v*/*v*) lactic acid aqueous solution under visible light illumination (120 mW·cm^{-2}) for 1 h.

References

(1) Ilic, S.; Zoric, M. R.; Kadel, U. P.; Huang, Y.; Glusac, K. D., Metal-free motifs for solar fuel applications. *Annu. Rev. Phys. Chem.* **2017,** 68, 305-331.

(2) Crespo-Quesada, M.; Reisner, E., Emerging approaches to stabilise photocorrodible electrodes and catalysts for solar fuel applications. *Energy Environ. Sci.* **2017,** 10, 1116-1127.

(3) Cho, J.; Sheng, A.; Suwandaratne, N.; Wangoh, L.; Andrews, J. L.; Zhang, P.; Piper, L. F.; Watson, D. F.; Banerjee, S., The Middle Road Less Taken: Electronic-Structure-Inspired Design of Hybrid Photocatalytic Platforms for Solar Fuel Generation. *Acc. Chem. Res.* **2018**.

(4) Cook, T. R.; Dogutan, D. K.; Reece, S. Y.; Surendranath, Y.; Teets, T. S.; Nocera, D. G., Solar energy supply and storage for the legacy and nonlegacy worlds. *Chem. Rev.* **2010,** 110, 6474-6502.

(5) Su, J.; Vayssieres, L., A place in the sun for artificial photosynthesis? *ACS Energy Letters* **2016,** 1, 121-135.

(6) Selinsky, R. S.; Ding, Q.; Faber, M. S.; Wright, J. C.; Jin, S., Quantum dot nanoscale heterostructures for solar energy conversion. *Chem. Soc. Rev.* **2013,** 42, 2963-2985.

(7) He, R.; Xu, D.; Cheng, B.; Yu, J.; Ho, W., Review on nanoscale Bi-based photocatalysts. *Nanoscale Horiz.* **2018,** 3, 464-504.

(8) Razek, S. A.; Popeil, M. R.; Wangoh, L.; Rana, J.; Suwandaratne, N.; Andrews, J. L.; Watson, D. F.; Banerjee, S.; Piper, L. F., Designing catalysts for water splitting based on electronic structure considerations. *Electron. Struct.* **2020,** 2, 023001.

(9) Mak, K. F.; Lee, C.; Hone, J.; Shan, J.; Heinz, T. F., Atomically thin MoS_2: a new direct-gap semiconductor. *Phys. Rev. Lett.* **2010,** 105, 136805.

(10) Voiry, D.; Salehi, M.; Silva, R.; Fujita, T.; Chen, M.; Asefa, T.; Shenoy, V. B.; Eda, G.; Chhowalla, M., Conducting MoS_2 nanosheets as catalysts for hydrogen evolution reaction. *Nano letters* **2013,** 13, 6222-6227.

(11) Choi, Y.-H.; Lee, J.; Parija, A.; Cho, J.; Verkhoturov, S. V.; Al-Hashimi, M.; Fang, L.; Banerjee, S., An in Situ Sulfidation Approach for the Integration of MoS_2 Nanosheets on Carbon Fiber Paper and the Modulation of Its Electrocatalytic Activity by Interfacing with *n*C60. *ACS Catal.* **2016,** 6, 6246-6254.

(12) Parija, A.; Choi, Y.-H.; Liu, Z.; Andrews, J. L.; De Jesus, L. R.; Fakra, S. C.; Al-Hashimi, M.; Batteas, J. D.; Prendergast, D.; Banerjee, S., Mapping Catalytically Relevant Edge Electronic States of MoS_2. *ACS Cent. Sci.* **2018**.

(13) Choi, Y.-H.; Cho, J.; Lunsford, A. M.; Al-Hashimi, M.; Fang, L.; Banerjee, S., Mapping the electrocatalytic activity of MoS_2 across its amorphous to crystalline transition. *J. Mater. Chem. A* **2017,** 5, 5129-5141.

(14) Wang, Y.; Zhang, Z.; Zhang, L.; Luo, Z.; Shen, J.; Lin, H.; Long, J.; Wu, J. C.; Fu, X.; Wang, X., Visible-Light Driven Overall Conversion of CO_2 and H_2O to CH_4 and O_2 on 3D-SiC@ 2D-MoS_2 Heterostructure. *J. Am. Chem. Soc.* **2018,** 140, 14595-14598.

(15) Li, K.; An, X.; Park, K. H.; Khraisheh, M.; Tang, J., A critical review of CO_2 photoconversion: catalysts and reactors. *Catal. Today* **2014,** 224, 3-12.

(16) Pelcher, K. E.; Milleville, C. C.; Wangoh, L. W.; Cho, J.; Sheng, A.; Chauhan, S.; Sfeir, M. Y.; Piper, L. F.; Watson, D. F.; Banerjee, S., Programming Interfacial Energetic Offsets and Charge Transfer in β-$Pb_{0.33}V_2O_5$/Quantum-Dot Heterostructures: Tuning Valence Band Edges to Overlap with Midgap States. *J. Phys. Chem. C* **2016**.

(17) Andrews, J. L.; Cho, J.; Wangoh, L.; Suwandaratne, N.; Sheng, A.; Chauhan, S.; Nieto, K.; Mohr, A.; Kadassery, K. J.; Popeil, M. R., Hole Extraction by Design in Photocatalytic Architectures Interfacing CdSe Quantum Dots with Topochemically Stabilized Tin Vanadium Oxide. *J. Am. Chem. Soc.* **2018,** 140, 17163-17174.

(18) Zhang, K.; Zhang, T.; Cheng, G.; Li, T.; Wang, S.; Wei, W.; Zhou, X.; Yu, W.; Sun, Y.; Wang, P., Interlayer transition and infrared photodetection in atomically thin type-II $MoTe_2$/MoS_2 van der Waals heterostructures. *ACS nano* **2016,** 10, 3852-3858.

(19) Rivera, P.; Schaibley, J. R.; Jones, A. M.; Ross, J. S.; Wu, S.; Aivazian, G.; Klement, P.; Seyler, K.; Clark, G.; Ghimire, N. J., Observation of long-lived interlayer excitons in monolayer $MoSe_2$–WSe_2 heterostructures. *Nat. Commun.* **2015,** 6, 6242.

(20) Chen, H.; Wen, X.; Zhang, J.; Wu, T.; Gong, Y.; Zhang, X.; Yuan, J.; Yi, C.; Lou, J.; Ajayan, P. M., Ultrafast formation of interlayer hot excitons in atomically thin MoS_2/WS_2 heterostructures. *Nat. Commun.* **2016,** 7, 12512.

(21) Hong, X.; Kim, J.; Shi, S.-F.; Zhang, Y.; Jin, C.; Sun, Y.; Tongay, S.; Wu, J.; Zhang, Y.; Wang, F., Ultrafast charge transfer in atomically thin MoS_2/WS_2 heterostructures. *Nat. Nanotechnol.* **2014,** 9, 682.

(22) Chauhan, S.; Sheng, A.; Cho, J.; Razek, S. A.; Suwandaratne, N.; Sfeir, M. Y.; Piper, L. F.; Banerjee, S.; Watson, D. F., Type-II heterostructures of α-V_2O_5 nanowires interfaced with cadmium chalcogenide quantum dots: Programmable energetic offsets, ultrafast charge transfer, and photocatalytic hydrogen evolution. *J. Chem. Phys.* **2019,** 151, 224702.

(23) Tsai, M.-L.; Su, S.-H.; Chang, J.-K.; Tsai, D.-S.; Chen, C.-H.; Wu, C.-I.; Li, L.-J.; Chen, L.-J.; He, J.-H., Monolayer MoS_2 heterojunction solar cells. *ACS nano* **2014,** 8, 8317-8322.

(24) Liu, Y.; Yu, Y.-X.; Zhang, W.-D., MoS_2/CdS heterojunction with high photoelectrochemical activity for H_2 evolution under visible light: the role of MoS_2. *J. Phys. Chem. C* **2013,** 117, 12949-12957.

(25) Pesci, F. M.; Sokolikova, M. S.; Grotta, C.; Sherrell, P. C.; Reale, F.; Sharda, K.; Ni, N.; Palczynski, P.; Mattevi, C., MoS_2/WS_2 heterojunction for photoelectrochemical water oxidation. *ACS Catal.* **2017,** 7, 4990-4998.

(26) Cho, J.; Jung, Y. K.; Lee, J.-K., Kinetic studies on the formation of various II–VI semiconductor nanocrystals and synthesis of gradient alloy quantum dots emitting in the entire visible range. *J. Mater. Chem.* **2012,** 22, 10827-10833.

(27) Cho, J.; Jung, Y. K.; Lee, J.-K.; Jung, H.-S., Highly efficient Blue-Emitting CdSe-derived Core/Shell Gradient Alloy Quantum Dots with Improved Photoluminescent Quantum Yield and Enhanced Photostability. *Langmuir* **2017,** 33, 3711-3719.

(28) Li, H.; Wu, J.; Yin, Z.; Zhang, H., Preparation and applications of mechanically exfoliated single-layer and multilayer MoS_2 and WSe_2 nanosheets. *Acc. Chem. Res.* **2014,** 47, 1067-1075.

(29) Coleman, J. N.; Lotya, M.; O'Neill, A.; Bergin, S. D.; King, P. J.; Khan, U.; Young, K.; Gaucher, A.; De, S.; Smith, R. J., Two-dimensional nanosheets produced by liquid exfoliation of layered materials. *Science* **2011,** 331, 568-571.

(30) Jawaid, A.; Nepal, D.; Park, K.; Jespersen, M.; Qualley, A.; Mirau, P.; Drummy, L. F.; Vaia, R. A., Mechanism for liquid phase exfoliation of MoS_2. *Chem. Mater.* **2015,** 28, 337-348.

(31) Xie, J.; Zhang, H.; Li, S.; Wang, R.; Sun, X.; Zhou, M.; Zhou, J.; Lou, X. W. D.; Xie, Y., Defect-rich MoS_2 ultrathin nanosheets with additional active edge sites for enhanced electrocatalytic hydrogen evolution. *Adv. Mater.* **2013,** 25, 5807-5813.

(32) Wang, J.; Isshiki, M., Wide-bandgap II–VI semiconductors: growth and properties. In *Springer handbook of electronic and photonic materials*, Springer: 2006; pp 325-342.

(33) Pelcher, K. E.; Milleville, C. C.; Wangoh, L.; Chauhan, S.; Crawley, M. R.; Marley, P. M.; Piper, L. F.; Watson, D. F.; Banerjee, S., Integrating β-$Pb_{0.33}V_2O_5$ Nanowires with CdSe Quantum Dots: Toward Nanoscale Heterostructures with Tunable Interfacial Energetic Offsets for Charge Transfer. *Chem. Mater.* **2015,** 27, 2468-2479.

(34) Aleithan, S. H.; Livshits, M. Y.; Khadka, S.; Rack, J. J.; Kordesch, M. E.; Stinaff, E., Broadband femtosecond transient absorption spectroscopy for a CVD MoS_2 monolayer. *Phys. Rev. B* **2016,** 94, 035445.

(35) Shi, H.; Yan, R.; Bertolazzi, S.; Brivio, J.; Gao, B.; Kis, A.; Jena, D.; Xing, H. G.; Huang, L., Exciton dynamics in suspended monolayer and few-layer MoS_2 2D crystals. *ACS nano* **2013,** 7, 1072-1080.

(36) Milleville, C. C.; Pelcher, K. E.; Sfeir, M. Y.; Banerjee, S.; Watson, D. F., Directional Charge Transfer Mediated by Mid-Gap States: A Transient Absorption Spectroscopy Study of CdSe Quantum Dot/β-$Pb_{0.33}V_2O_5$ Heterostructures. *J. Phys. Chem. C* **2016,** 120, 5221-5232.

(37) Li, H.; Zhang, Q.; Yap, C. C. R.; Tay, B. K.; Edwin, T. H. T.; Olivier, A.; Baillargeat, D., From bulk to monolayer MoS_2: evolution of Raman scattering. *Adv. Funct. Mater.* **2012,** 22, 1385-1390.

(38) Carvalho, B. R.; Wang, Y.; Mignuzzi, S.; Roy, D.; Terrones, M.; Fantini, C.; Crespi, V. H.; Malard, L. M.; Pimenta, M. A., Intervalley scattering by acoustic phonons in two-dimensional MoS_2 revealed by double-resonance Raman spectroscopy. *Nat. Commun.* **2017,** 8, 14670.

(39) Liang, K.; Hughes, G.; Chianelli, R., UPS investigation of poorly crystallized MoS_2. *J. Vac. Sci. Technol. A* **1984,** 2, 991-994.

(40) Tao, J.; Chai, J.; Lu, X.; Wong, L. M.; Wong, T. I.; Pan, J.; Xiong, Q.; Chi, D.; Wang, S., Growth of wafer-scale MoS 2 monolayer by magnetron sputtering. *Nanoscale* **2015,** 7, 2497-2503.

(41) Menéndez-Proupin, E.; Amézaga, A.; Hernández, N. C., Electronic structure of CdTe using GGA+ USIC. *Physica B Condens Matter.* **2014,** 452, 119-123.

(42) Scofield, J. H. *Theoretical photoionization cross sections from 1 to 1500 keV*; California Univ., Livermore. Lawrence Livermore Lab.: 1973.

(43) Yuan, C.; Li, L.; Huang, J.; Ning, Z.; Sun, L.; Ågren, H., Improving the photocurrent in quantum-dot-sensitized solar cells by employing alloy $Pb_xCd_{1-x}S$ quantum dots as photosensitizers. *Nanomaterials* **2016,** 6, 97.

(44) Wei, X.-L.; Zhang, H.; Guo, G.-C.; Li, X.-B.; Lau, W.-M.; Liu, L.-M., Modulating the atomic and electronic structures through alloying and heterostructure of single-layer MoS_2. *J. Mater. Chem. A* **2014,** 2, 2101-2109.

(45) Van de Walle, C. G.; Neugebauer, J., Universal alignment of hydrogen levels in semiconductors, insulators and solutions. *Nature* **2003,** 423, 626.

(46) Pogna, E. A.; Marsili, M.; De Fazio, D.; Dal Conte, S.; Manzoni, C.; Sangalli, D.; Yoon, D.; Lombardo, A.; Ferrari, A. C.; Marini, A., Photo-induced bandgap renormalization governs the ultrafast response of single-layer MoS_2. *ACS nano* **2016,** 10, 1182-1188.

(47) Kime, G.; Leontiadou, M. A.; Brent, J. R.; Savjani, N.; O'Brien, P.; Binks, D., Ultrafast Charge Dynamics in Dispersions of Monolayer MoS_2 Nanosheets. *J. Phys. Chem. C* **2017,** 121, 22415-22421.

(48) Bettis Homan, S.; Sangwan, V. K.; Balla, I.; Bergeron, H.; Weiss, E. A.; Hersam, M. C., Ultrafast exciton dissociation and long-lived charge separation in a photovoltaic pentacene–MoS_2 van der Waals heterojunction.

Nano letters **2016,** 17, 164-169.

(49) Raja, A.; Selig, M.; Berghäuser, G.; Yu, J.; Hill, H. M.; Rigosi, A. F.; Brus, L. E.; Knorr, A.; Heinz, T. F.; Malic, E., Enhancement of Exciton–Phonon Scattering from Monolayer to Bilayer WS_2. *Nano letters* **2018,** 18, 6135-6143.

(50) Palummo, M.; Bernardi, M.; Grossman, J. C., Exciton radiative lifetimes in two-dimensional transition metal dichalcogenides. *Nano lett.* **2015,** 15, 2794-2800.

(51) Wang, H.; Zhang, C.; Rana, F., Ultrafast dynamics of defect-assisted electron–hole recombination in monolayer MoS_2. *Nano lett.* **2014,** 15, 339-345.

(52) Han, B.; Hu, Y. H., MoS2 as a co-catalyst for photocatalytic hydrogen production from water. *Energy Science & Engineering* **2016,** 4, 285-304.

(53) Schwarz, K.; Blaha, P., Solid state calculations using WIEN2k. *Comput. Mater. Sci.* **2003,** 28, 259-273.

(54) Blaha, P.; Schwarz, K.; Madsen, G.; Kvasnicka, D.; Luitz, J., WIEN2k (Vienna University of Technology Austria, 2002). **2010**.